Geophys. J. Int. (2009) **177,** 1037–1049 doi: 10.1111/j.1365-246X.2008.04084.x

Seismic velocities in Southern Tibet lower crust: a receiver function approach for eclogite detection

Gérard Wittlinger,[1] Véronique Farra,[2] György Hetényi,[3] Jérôme Vergne[1] and John Nábělek[4]

[1] *EOST,* UMR-CNRS 7516, 5 *rue René Descartes,* 67084 *Strasbourg-Cedex, France*
[2] *IPG Paris,* UMR-CNRS 7154, *case* 89, 4 *place Jussieu* 75252, *Paris, France. E-mail: farra@ipgp.jussieu.fr*
[3] *Laboratoire de Géologie, Ecole Normale Supérieure,* UMR-CNRS 8538, 24 *rue Lhomond* 75005, *Paris, France*
[4] *College of Oceanic and Atmospheric Sciences, Oregon State University, Corvalis,* OR 97331, *USA*

Accepted 2008 December 16. Received 2008 December 15; in original form 2008 August 28

SUMMARY

Beneath the Tibet plateau, the deficit of crustal thickening with respect to what is expected from the plate tectonic constraints is thought to be absorbed either by lateral extrusion or by vertical rock-mass transfer. To nourish the unsettled debate of the relative importance of these two processes, we propose a new approach, based on the *S*-to-*P* and the *P*-to-*S* wave conversions, enabling the precise determination of the seismic velocities. The weighted amplitudes of the direct conversion and of reverberations are stacked at their predicted arrival times for various values of layer thickness and v_P/v_S ratio separately for two sets of *P*- and *S*-receiver functions. For each set of receiver functions, coherent stack gives the $v_P/\,v_S$ ratio and thickness for the considered layer (the grid search stacking method). The values of v_P/v_S ratio and layer thickness are functions of the velocity used for stacking the set of receiver functions, but using the *P*- and *S*-receiver functions allows us to solve this indetermination and to find the effective parameters of the layer: velocity v_S, $v_P/\,v_S$ ratio and thickness. We use a bootstrap resampling of the receiver function data sets to estimate the parameters uncertainties. For the Southern Lhasa Block, the migrated sections of both *P*- and *S*-receiver functions (Hi-CLIMB experiment data) show a layer in the lower crust that may be related to the lower Indian crust underplated beneath Tibet. With the grid search stacking method, high shear wave velocities ($v_S \sim$ 4.73 km s^{-1}) and low v_P/v_S ratios ($\sim$1.69) are detected in this layer. Such values are typical for high-grade eclogites, and the low v_P/v_S ratio precludes the confusion with mafic granulites. There is no evidence for partial eclogitization near and south of the Yarlung–Tsangpo Suture, and the about 19 km thick eclogitic layer extends northwards only to about the middle of the Lhasa terrane.

Key words: Composition of the continental crust; Body waves; Asia.

INTRODUCTION

Three main processes are thought to accommodate the India–Asia convergence in the Himalayas–Tibet, namely the crustal thickening, the crustal lateral extrusion and some vertical rock transfer/transformation. The latter, the vertical rock-mass transfer and/or transformation (England & Houseman 1989; Le Pichon *et al.* 1992) at the crust–mantle or lithosphere–asthenosphere boundaries remain until today weakly constrained by seismological direct measures. The thickening of the Tibetan crust appears to be less important than what is expected from the amount of shortening estimated from plate tectonic constraints. One can attribute this deficit to the presence, in the lower crust, of dense materials like eclogites that may founder in the mantle and/or may be transformed into granulites (Henry *et al.* 1997; Le Pichon *et al.* 1997) which contribute to the plateau raising, and/or to some lateral extrusion of the excess of crustal material (Tapponnier & Molnar 1977; Peltzer & Tapponnier 1988). The relative importance of these processes remains unsettled. The direct detection of the amount of eclogitization in the lower Tibetan crust is thus decisive to nourish the debate.

The detection with seismological tools of eclogites or other high-velocity and high-density rocks like mafic granulites, in the lower crust, remains a challenge. When using refraction–reflection profiling (Sapin *et al.* 1996; Haines *et al.* 2003; herein many other references), the eclogitic layer may be seen as part of the mantle since its seismic velocities are very similar to those of the upper mantle. In addition, the great depth and the rather small lateral extension of the presumed eclogitic layer in Tibet render its detection even more difficult when using the refraction–reflection profiling or the body wave or surface wave tomography. Recently, *P*- and *S*-wave traveltime inversions from local earthquakes recorded on a temporary network in Nepal and Southern Tibet reveal *P*-wave

velocities over 8.4 km s^{-1} in the upper most mantle beneath the Greater Himalaya (Monsalve *et al.* 2008). These high velocities are interpreted as resulting from the eclogitization of the Indian lower crust. When using receiver functions (RFs), both the ceiling and the base of the high-velocity layer are detected (Kind *et al.*, 2002; Wittlinger *et al.* 2004b; and others), but due to the lack of an absolute velocity determination with RFs the generally well-imaged 'doublet' cannot be unquestionably related to the eclogites (Schulte-Pelkum *et al.* 2005). This uncertainty can be greatly reduced when using gravity anomalies in order to constrain the density of the layer in question (Hetényi *et al.* 2007). Still, one would like to further discriminate with seismological tools between eclogites and mafic granulites since the transformation of the first into the latter is sometimes advocated to explain part of the uplift of the Tibet plateau (Le Pichon *et al.* 1997).

Relating seismic velocities observed in the whole crust to the composition of only the lower crust remains difficult and generally not univocal (Owen & Zandt 1997). Here, we describe a new method based simultaneously on the *P*-receiver functions (PRFs) and *S*-receiver functions (SRFs) and thus enabling the determination of the absolute shear wave velocity, the *P*-to-*S* velocity ratio and the thickness of the whole crust or of some specific crustal layers. We apply this method to the Hi-CLIMB data (Nábělek *et al.* 2005) and focus our investigation on the lower crust of the Lhasa terrane (Tibet) where there are strong evidences of the existence of significant amount of eclogitization (Sapin & Hirn 1997; Hetényi *et al.* 2007; Schulte-Pelkum *et al.* 2005).

METHOD AND ASSESSMENT WITH SYNTHETIC AND REAL DATA

Let us first consider a medium with one layer of thickness h, *P*-wave velocity v_P, *S*-wave velocity v_S and thus *P*-to-*S* velocity ratio κ, lying over a half-space. We have at our disposal PRFs and SRFs obtained for various incidence angles at a receiver located on the surface (Fig. 1 shows a synthetic example for a two-layered medium). Some differences exist between the two kinds of RFs (Wittlinger & Farra 2007), but the difference at the core of the method is that the ray parameters of the SRFs phases are substantially greater than the ray parameters of the PRFs phases.

Let us consider the differential traveltimes between the direct *P* wave (resp. *S* wave) and the converted *P*-to-*S* (resp. *S*-to-*P*) wave, and also the *Ppps* and *Psps* + *Ppss* (resp.*Sssp* and *Spsp* + *Sspp*) reverberations. In the plane-wave approximation, we can write:

$$t_{Ps} = h\left(\sqrt{\frac{1}{v_S^2} - p_P^2} - \sqrt{\frac{1}{v_S^2\kappa^2} - p_P^2}\right), \tag{1}$$

$$t_{Ppss,Psps} = 2h\sqrt{\frac{1}{v_S^2} - p_P^2}, \tag{2}$$

$$t_{Ppps} = h\left(\sqrt{\frac{1}{v_S^2} - p_P^2} + \sqrt{\frac{1}{v_S^2\kappa^2} - p_P^2}\right), \tag{3}$$

$$t_{Sp} = h\left(\sqrt{\frac{1}{v_S^2\kappa^2} - p_S^2} - \sqrt{\frac{1}{v_S^2} - p_S^2}\right), \tag{4}$$

$$t_{Sspp,Spsp} = 2h\sqrt{\frac{1}{v_S^2\kappa^2} - p_S^2}, \tag{5}$$

$$t_{Sssp} = h\left(\sqrt{\frac{1}{v_S^2\kappa^2} - p_S^2} + \sqrt{\frac{1}{v_S^2} - p_S^2}\right), \tag{6}$$

where p_P and p_S are the ray parameters of the considered *P* or *S* wave. The three differential traveltimes (1–3) (resp. 4–6) are not independent since expression (2) (resp. 5) is the sum of expressions (1) and (3), (resp. 4 and 6). For this reason, if only one kind of RFs is used, a trade-off between v_S, κ and h exists. Nevertheless, the simultaneous use of the PRFs and the SRFs suppresses this trade-off.

The 'grid search stacking method' of Zhu & Kanamori (2000) applied successively to the PRFs and the SRFs sums the weighted RFs amplitudes A_i of the converted *Ps* (resp. *Sp*) and of the reverberated *Ppps* and *Ppss* + *Psps* (resp. *Sssp* and *Sspp* + *Spsp*) phases at the predicted arrival times t_{Ps}, t_{Ppps}, $t_{Ppss,Psps}$ (resp. t_{Sp}, t_{Sssp}, $t_{Sspp,Spsp}$) for various values of thickness h and v_P/v_S ratio κ, assuming the *P*-wave velocity v_P (resp. the *S*-wave velocity v_S) as a known parameter (Fig. 2):

$$B_P(h,k) = \sum_{i=1}^{np}[w_{P1}A_i(t_{Ps}) + w_{P2}A_i(t_{Ppps}) - w_{P3}A_i(t_{Ppss,Psps})], \tag{7}$$

$$B_S(h,k) = \sum_{i=1}^{ns}[w_{S1}A_i(t_{Sp}) + w_{S2}A_i(t_{Sssp}) - w_{S3}A_i(t_{Sspp,Spsp})]. \tag{8}$$

In eqs (7) and (8), w_{P1}, w_{P2} and w_{P3} (resp. w_{S1}, w_{S2} and w_{S3}) are positive weights applied to the direct and to the reverberated phases, the negative sign before w_{P3} and w_{S3} takes into account the reversed sign of the *Ppss* + *Psps* and of the *Sspp* + *Spsp* multiples, *np* (resp. *ns*) is the total number of *P* (resp. *S*) receiver functions. The functions $B(h, \kappa)$ are plotted in the (h, κ) plane for values of h and κ varying, respectively, from h_1 to h_2 and κ_1 to κ_2 using a discrete mesh. The 'best' estimates of h and κ are obtained for the maximum value of $B(h, \kappa)$, corresponding to the coherent stack of the *Ps* phase (resp. the *Sp* phase) and reverberations (Fig. 2). Indeed, the layer thickness h and v_P/v_S ratio κ determined with the grid search stacking method depend on the velocity used for the stack. But, since the stack is performed along the differential traveltime curves, whatever the value of the stack velocity may be, the h- and κ-values we obtain give the closest fit between the theoretical differential traveltimes (calculated with eqs 1–3 or eqs 4–6) and the observed ones.

Combining now eqs (1) and (3) (resp. 4 and 6), we obtain the layer thickness h_P (resp. h_S) deduced from the PRFs (resp. SRFs) as a function of the shear wave velocity v_S:

$$h_P = \frac{v_S}{2}\sqrt{\frac{C_P}{1 - P_p^2 v_S^2}}, \tag{9}$$

$$h_S = \frac{v_S}{2}\sqrt{\frac{C_S}{1 - P_s^2 v_S^2}}, \tag{10}$$

where the coefficients $C_P = (t_{Ps} + t_{Ppps})^2$ and $C_S = (t_{Sp} - t_{Sssp})^2$ involve only the differential traveltimes.

Combining eqs (1) and (3) (resp. 4 and 6), we obtain the *P*-to-*S* velocity ratio κ_P (resp. κ_S) deduced from the PRFs (resp. SRFs) as a function of the shear wave velocity:

$$\kappa_P = \frac{1}{\sqrt{D_P + v_S^2 p_p^2(1 - D_P)}}, \tag{11}$$

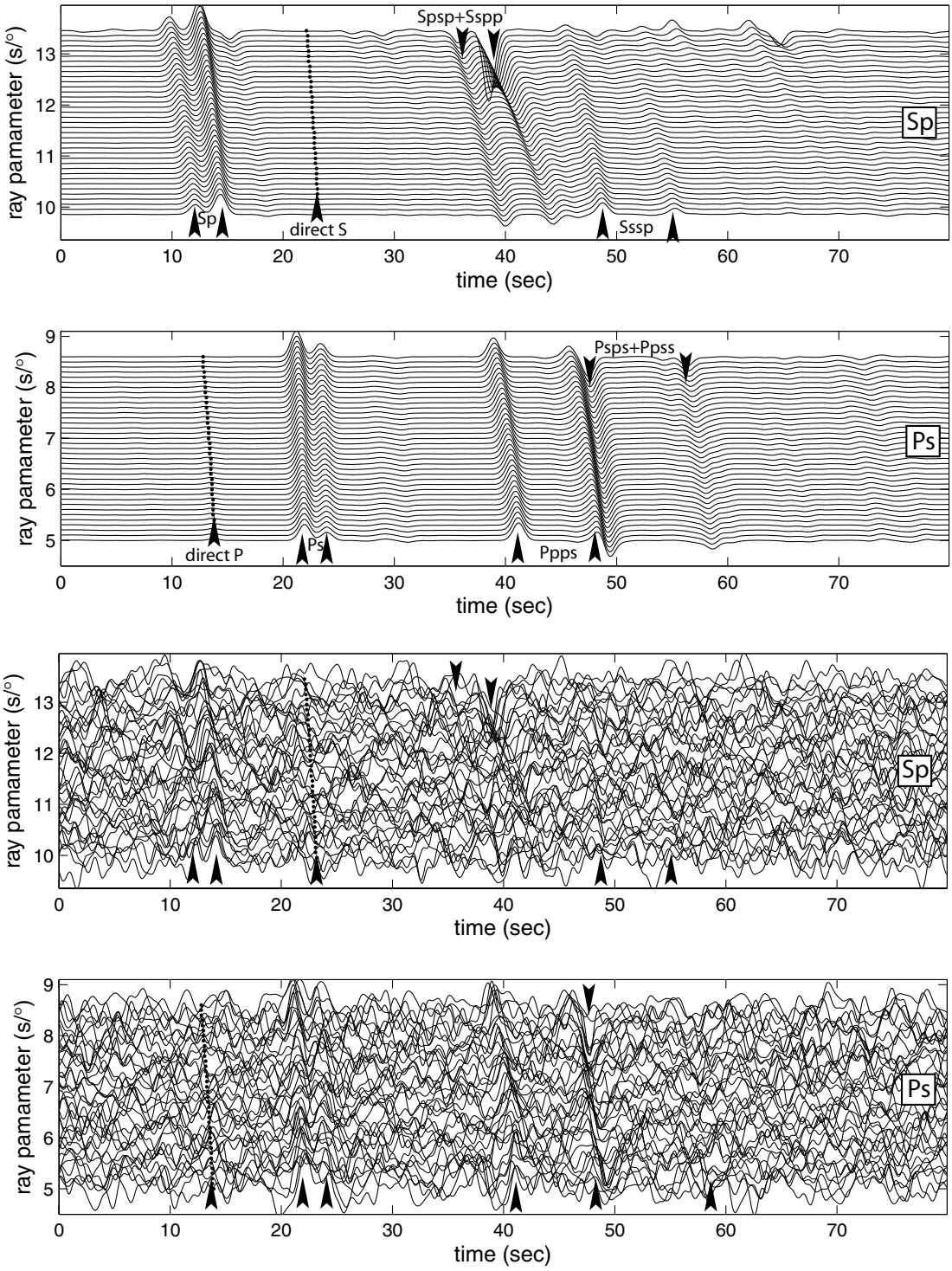

Figure 1. Synthetic PRFs and SRFs computed using the reference model given in Table 1 and plotted for increasing ray parameters spanning from 5 to 8.6 s deg^{-1} (resp. 9.8–13.5 s deg^{-1}) for the PRFs (resp. the SRFs). Subplots (a) and (b) RFs without additional random noise; subplots (c) and (d) RFs with additional noise. The random noise on each RF is generated by a sum of sinusoids each one having random frequency (spanning from 0.125 to 1 Hz), amplitude (around a given mean amplitude) and phase. In subplots (c) and (d), the converted phases are almost concealed by the added strong random noise.

$$\kappa_S = \frac{1}{\sqrt{D_S + v_s^2 p_s^2 (1 - D_S)}}, \tag{12}$$

where the coefficients $D_P = (\frac{t_{Ppps} - t_{Ps}}{t_{Ppps} + t_{Ps}})^2$ and $D_S = (\frac{t_{Sssp} + t_{Sp}}{t_{Sssp} - t_{Sp}})^2$involve again only the differential traveltimes.

Numerical evaluation of expressions (9) to (12) shows (see Fig. 3) that h and κ are quite linearly related to v_S. The $\kappa_P(v_S)$ and $\kappa_S(v_S)$ curves are frankly secant if the ray parameters p_P and p_S are different (see Fig. 3), which is generally the case, as, on average, for PRFs $p_P \sim 6.5$ and for SRFs $p_S \sim 11.5$ s deg^{-1}. The coefficients C_P and D_P in eqs (9) and (11) (resp. C_S and D_S in eqs 10 and 12)

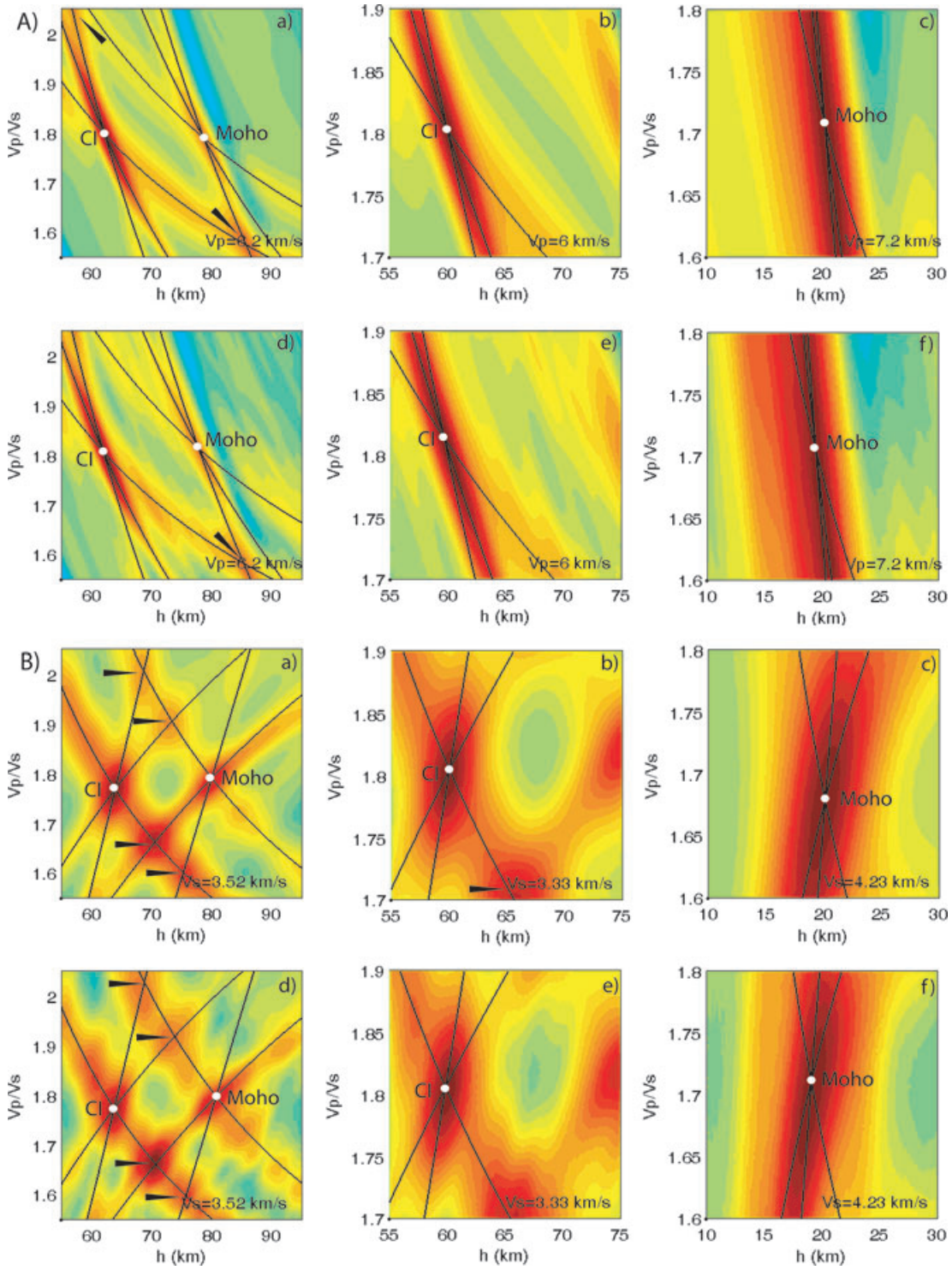

Figure 2. Grid search stacking in the (h, κ) plane of the synthetic PRFs (A) and SRFs (B) displayed in Fig. 1. Subplots (a–c) correspond to the raw RFs without additional random noise and subplots (d–f) to the noisy RFs. The value of the stack velocity is indicated on each subplot in the lower right corner. Numerous spurious maximums are observed especially for the SRFs (B) (little black pointers) generated by the association of the direct conversion on a given interface with the reverberations on other interfaces. White dots show the maximums corresponding to the Moho and to the CI. The respective contributions of the direct conversions and of the two strongest reverberations are underlined thin black lines. Subplots in the left-hand column involve CI and Moho, subplots in the middle column are the grid search stacking focused on the upper layer (CI) and subplots in the right-hand column are the grid search stacking restricted to the lower layer (Moho interface) using the 'layer stripping approach', and the values h, κ and v_S obtained for the upper layer.

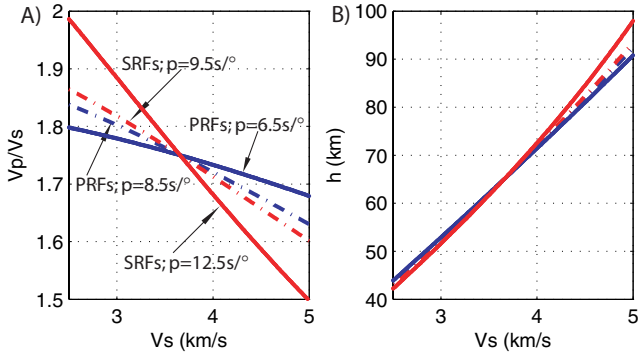

Figure 3. Theoretical $\kappa(v_S)$ (A) and $h(v_S)$ (B) curves for a 65 km thick crust with $\kappa = 1.75$ and $v_S = 3.657$ km s^{-1} using eqs (9)–(12). Red (resp. blue) solid lines stand for the SRFs, eqs (10) and (12) with $p_S = 12.5$ s deg^{-1} (resp. for the PRFs, eqs (9) and (11) with $p_P = 6.5$ s deg^{-1}). The broken lines stand for the $\kappa(v_S)$ and $h(v_S)$ curves obtained with quite similar ray parameters for the PRFs and the SRFs, $p_S = 9.5$ s deg^{-1} and $p_P = 8.5$s deg^{-1}; this shows that the ray parameters of the *P* and *S* waves should be strongly different to give a clear intersection of the $\kappa(v_S)$ curves. Plot (B) shows that the $h(v_S)$ curves never crosscut frankly whatever the ray parameters be.

are determined from the values (v_S, h, κ) obtained with the 'grid search stacking' of the PRFs (resp. of the SRFs). The value of p_P (resp. p_S) is taken as the average ray parameter of the PRFs (resp. SRFs) data set. The crosscutting of the $\kappa_P(v_S)$ and $\kappa_S(v_S)$ curves gives thus the effective velocity of the layer and the v_P/v_S ratio. By equating eqs (11) and (12), we obtained the effective shear velocity:

$$v_S = \sqrt{\frac{D_S - D_P}{p_P^2(1 - D_P) - p_S^2(1 - D_S)}}. \tag{13}$$

In turn, using the v_S value in eq. (11) or (12) the effective κ-ratio follows. Unfortunately, the h_P and h_S curves are never frankly secant (see Fig. 3) and the layer thickness can only be obtained by reporting the effective velocity v_S deduced from the intersection of the $\kappa(v_S)$ curves on the $h(v_S)$ curves.

We assess this method using synthetic PRFs and SRFs computed for an isotropic, two-layered crust (the model is given as 'reference model' in Table 1, the synthetics are plotted in Fig. 1 without and with additional random noise). The ray parameters of the PRFs (resp. of the SRFs) span from 5.0 to 8.6 s deg^{-1} (resp. from 9.8 to 13.5 s deg^{-1}) and correspond approximately to the ray parameters of the real data set we use in the following. We take a two-layered crust to probe the resolution of the method and to show that if applied to a stack of layers this method allows the unwrapping of the entire crust, layer after layer. This stacking process is only marginally affected by noisy RFs, since the noise is not spatially coherent along the predicted differential traveltime curves, given in eqs 1 to 6, along which we stack. The strong random noise we added to both the *P* and *S* synthetic receiver functions (Figs 1c and d), though concealing the direct conversions and the multiples, has only very weak effect on the stack functions (Figs 2A: d, e and f and 2B: d, e and f). As the grid search stacking method takes advantage of the spatial lateral coherence of the direct conversions and of the multiples, the method is basically robust.

When applying this method to a stack of several layers, we use a 'layer stripping approach' to determine the velocities and thickness for each layer, sequentially from surface to depth. We use the results (velocities and thickness) gained previously for all the layers located above the considered layer. The differential traveltimes of the *Ps* and *Sp* phases and of the corresponding reverberated phases propagating in the piling of n layers are the sums, over the n layers, of the relations (1)–(6). The grid search stacking is used to determine the parameters h, κ and v_S of the nth layer knowing the parameters h, κ and v_S of the $(n-1)$ upper layers (Fig. 2). As the parameter errors are propagated from one layer to the following one with the layer stripping approach, at this stage of investigation, we consider only two layers in the following sections.

When performing the 'grid search stacking' with real data, two kinds of errors are made in addition to the usual picking error of the maximum of the stack function. The first kind ensues from the misinterpretation of the local optimums of the stack function (see Fig. 2, black pointers). This misinterpretation happens if the retained optimum is the addition of the direct conversion at a given interface with the multiples generated at another interface. This error leads to very strong discrepancy between PRFs' and SRFs' results; the $\kappa_P(v_S)$ and $\kappa_S(v_S)$ curves are no longer secant in an acceptable (v_S, κ) domain. Such errors can be avoided by a careful interpretation of the grid search diagrams with the help of some a priori constraints fixing the upper and lower bounds of the crustal velocities, the *P*-to-*S* velocity ratio and the layer thickness. The second kind of error follows from the seismic noise itself and from the deconvolution noise blemishing both the RFs. This error and the picking error are evaluated by using the 'bootstrap' sampling method applied to the set of RFs that are selected for the stack. The 'bootstrap' sampling of the RFs sets allows generating numerous (we choose here 40) grid search diagrams similar to those shown in Fig. 2 using always the same value of the stack velocity. On each diagram, we pick the h- and κ-values of the maximum and evaluate the coefficients (C_P and D_P) if PRFs' data are considered or (C_S and D_S) for SRFs' data; the value of p_P or p_S is taken as the average ray parameter of the considered RFs set. In this way, we plot two bundles of 40 $\kappa(v_S)$ and $h(v_S)$ curves (Figs 4a and b, 5a and b, subplots a and b). The intersections of the $\kappa_P(v_S)$ and $\kappa_S(v_S)$

Table 1. Estimates of layer parameters (thickness, velocities and velocity-ratio) obtained with the 'layer stripping approach' for synthetic data with and without added random noise and with a dipping interface.

Synthetic without noise	Synthetic with (strong) noise	Synthetic without noise and with a dipping CI	Reference model
Upper crust	**Upper crust**	**Upper crust**	**Upper crust**
$h_1 = 60.1 \pm 0.2$ km	$h_1 = 60.7 \pm 0.6$ km	$h_1 = 61.6 \pm 1.8$ km	$h_1 = 60.0$ km
$v_{S1} = 3.34 \pm 0.01$ km s^{-1}	$v_{S1} = 3.36 \pm 0.04$ km s^{-1}	$v_{S1} = 3.58 \pm 0.02$ km s^{-1}	$v_{S1} = 3.33$ km s^{-1}
$v_{P1} = 6.02 \pm 0.028$ km s^{-1}	$v_{P1} = 6.05 \pm 0.10$ km s^{-1}	$v_{P1} = 6.47 \pm 0.05$ km s^{-1}	$v_{P1} = 6.00$ km s^{-1}
$\kappa_1 = 1.803 \pm 0.003$	$\kappa_1 = 1.802 \pm 0.008$	$\kappa_1 = 1.807 \pm 0.003$	$\kappa_1 = 1.800$
Lower crust	**Lower crust**	**Lower crust**	**Lower crust**
$h_2 = 19.5 \pm 0.6$ km	$h_2 = 19.3 \pm 2.2$ km	$h_2 = 21.7 \pm 2.4$ km	$h_2 = 20.0$ km
$v_{S2} = 4.16 \pm 0.11$ km s^{-1}	$v_{S2} = 4.17 \pm 0.42$ km s^{-1}	$v_{S2} = 4.29 \pm 0.19$ km s^{-1}	$v_{S2} = 4.23$ km s^{-1}
$v_{P2} = 7.13 \pm 0.119$ km s^{-1}	$v_{P2} = 7.21 \pm 1.14$ km s^{-1}	$v_{P2} = 7.41 \pm 0.44$ km s^{-1}	$v_{P2} = 7.20$ km s^{-1}
$\kappa_2 = 1.714 \pm 0.024$	$\kappa_2 = 1.723 \pm 0.052$	$\kappa_2 = 1.727 \pm 0.025$	$\kappa_2 = 1.702$

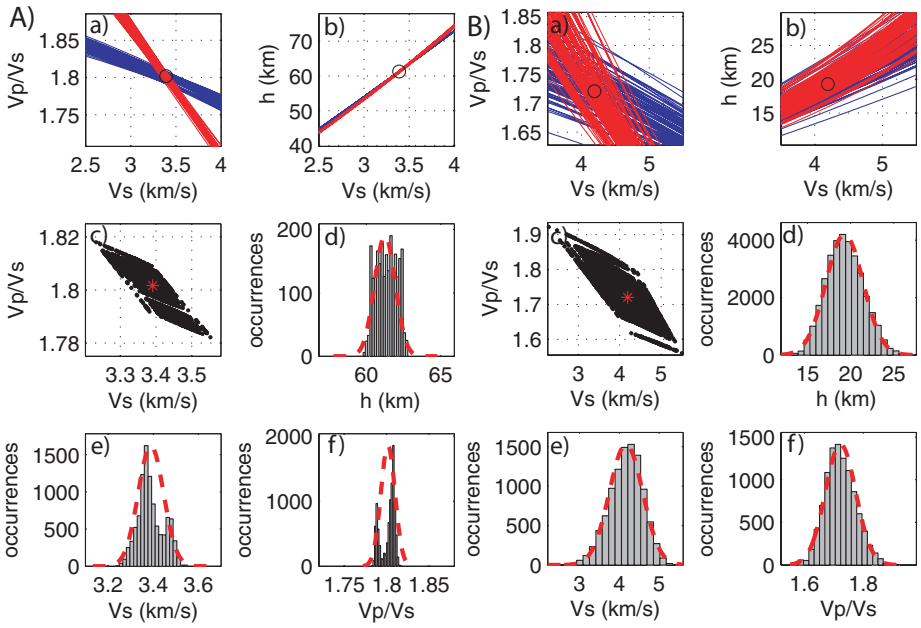

Figure 4. Shear velocity v_S, v_P/v_S ratio κ and layer thickness h determination on synthetic data with the strong additional noise as plotted in Figs 1c and d, (A) is relevant for the UCL and (B) for the lower crustal layer (the 'layer stripping approach'). The subplots (c) are enlargements of the $\kappa(v_S)$ curves intersections and give all the possible v_S and κ-values. In subplots (a) and (b), the red (resp. blue) colour stands for the SRFs (resp. the PRFs) results. The curve in red broken lines in subplots (d), (resp. e and f) is the Gaussian adjustment, using the estimated mean and variance of the corresponding histogram of all possible h (resp. v_S, κ) values.

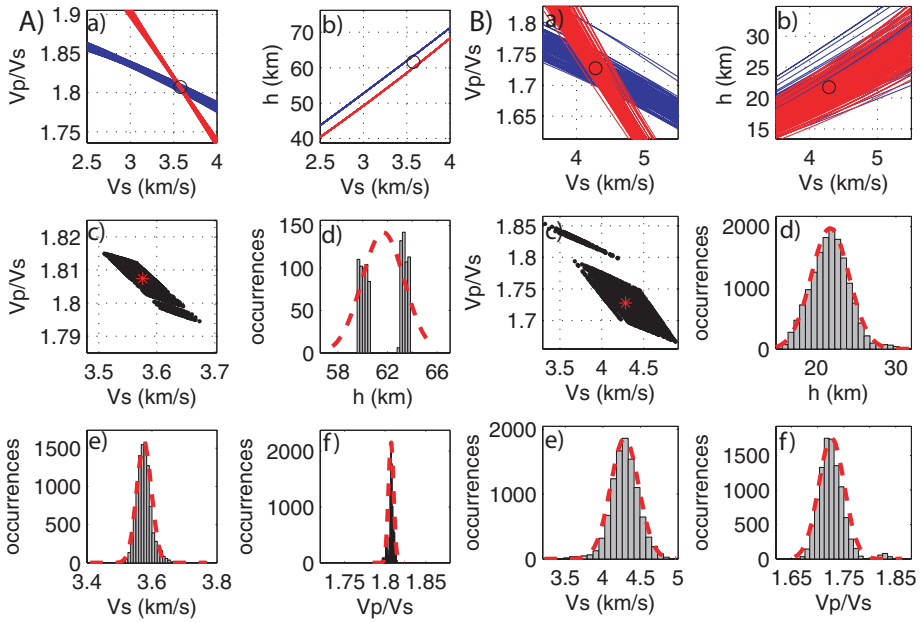

Figure 5. Same as Fig. 4 for synthetic data without noise, but computed in a model with a 5° dipping CI.

curves (subplots c of Figs 4 and 5 show an enlargement) give all the possible values of the effective shear velocity v_S and of the P-to-S velocity ratio κ and provide an estimation of their mean value and standard deviation. The histograms of the v_S and κ-values (Figs 4a and b, 5a and b, subplots e and f) corresponding to the intersections in the (v_S, κ) plane of the $\kappa_P(v_S)$ and $\kappa_S(v_S)$ curves do not always follow a strictly Gaussian distribution, but show that the mean and standard deviations are fairly good estimates of v_S and κ and of the errors made on these parameters. The histogram of the h-values (Figs 4a and b, 5a and b, subplots d) corresponds to the $h_P(v_S)$ and $h_S(v_S)$ values obtained for all the v_S values inferred from the intersections of the $\kappa_P(v_S)$ and $\kappa_S(v_S)$ curves. As the $h_P(v_S)$ and $h_S(v_S)$ curves do not intersect frankly, the histogram is rather bimodal than frankly Gaussian. However, again, the histogram gives a reasonably good estimate of the h-value and its error. Table 1 shows that for the synthetic data, without and even with strong noise, the model is quite exactly retrieved. Furthermore, we also test the outcome of the determination of v_S, κ and h of a 5° dipping crustal interface (CI). While the dip of an interface has only marginal effect on the grid search stacking results for the PRFs—since their ray

parameters are quite small (∼6.4 s deg^{-1})—the SRFs grid search results are much more severely affected because their ray parameters are greater (∼11.5 s deg^{-1}). Fig. 5 shows the results obtained with synthetic RFs computed for a model similar to the reference model given in Table 1, but with a 5° dip of the CI. We assume that the incident rays are coming from the side where the dipping interface is the shallowest. This is the worst case for the SRFs, as the ray paths of the multiples have their length quite increased and sample different depths of the interface. The parameters v_S, κ and h are reasonably well estimated in the two layers (see Table 1). In any case, the grid search stacking method should be used carefully if a strongly dipping layer is revealed for instance on the migrated sections. In the second part of the paper, we apply the grid search stacking method to Hi-CLIMB data set of Southern Tibet at places where the CI and the Moho are quite horizontal. The discrepancy between the layer thickness (Fig. 5A–b and d) obtained with the PRFs and with the SRFs appears as a good testimony of the presence of a dipping interface. In addition, these tests emphasize that (1) the $h(v_S)$ plot cannot be used to determine the actual velocity, and the interface depth can only be obtained after reporting the v_S value determined with the $\kappa(v_S)$ plot and (2) the maximums of the stack function in the (h, κ) diagrams should be carefully identified before picking especially on the diagrams obtained with the SRFs because spurious optimums can exist.

We now apply this method combined with the 'layer stripping approach' to part of the data set gained during the Hi-CLIMB experiment (Nábělek *et al.* 2005; Fig. 6). Due to the noise present in real data we use the RFs obtained at about five to 10 successive stations to compute one grid search diagram; typically this corresponds for the Hi-CLIMB experiment data to ∼500 SRFs and ∼1250 PRFs for each diagram. This introduces a spatial smoothing over ∼75 to ∼125 km of lateral extension, and the precise determination of the three parameters suffers from this smoothing if the interfaces are dipping (Lombardi *et al.* 2008). Here, we tackle further, using the Hi-CLIMB data set with the conversions at a CI and at the Moho, both clearly visible beneath the Southern Lhasa terrane on the two migrated sections shown in Fig. 7. These two interfaces define two superposed crustal layers, the upper crustal layer (UCL) and the lower crustal layer. The grid search stacking method is applied first to the CI and gives the mean value and the standard deviation of the thickness h, the velocity v_S and the κ-value of the UCL. In accordance with the ' layer stripping approach', the grid search stacking

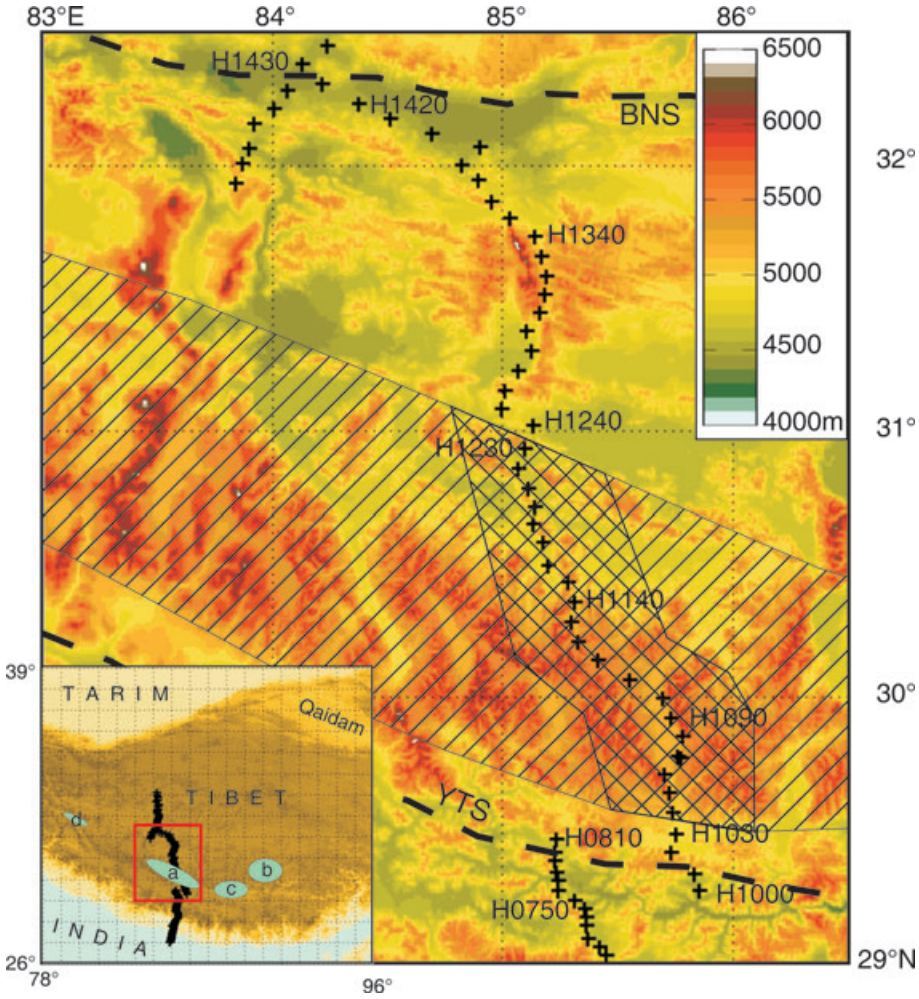

Figure 6. The Hi-CLIMB profile through the Tibet and the Lhasa terrane (equidistant cylindrical projection). The red rectangle in the insert corresponds to the studied area. The blue ellipses indicate approximately the places where the 'doublet' in the lower crust has been observed with RF migrations: (a) in this study, (b) with INDEPTH data, (c) with HIMNT data and d) with Sino–French data. The crisscrossed hatched area corresponds approximately to the area where the high velocities in the lower crust are measured using the Hi-CLIMB data. The simply hatched area corresponds to the region where the high-velocity layer is presumed to extend. The mean elevation of this hatched area is ∼440 m higher than the mean elevation of the northern part of the Lhasa terrane.

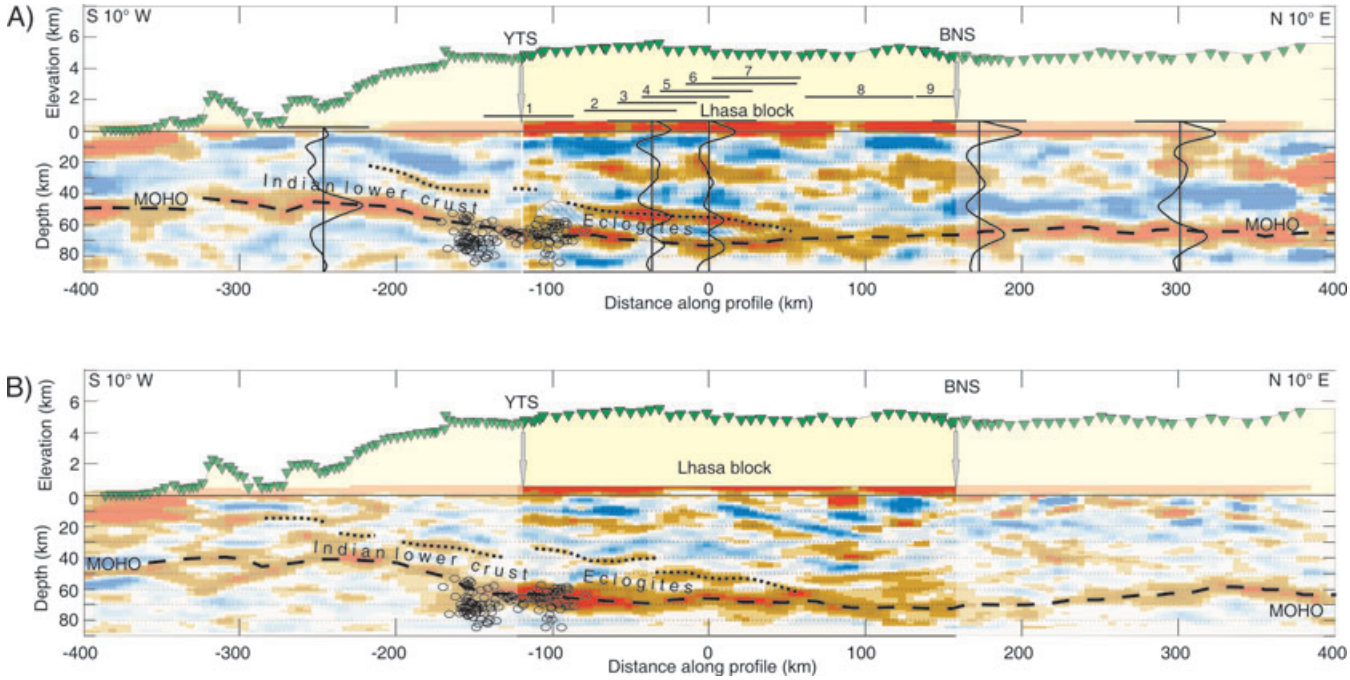

Figure 7. CCP migrated vertical sections oriented S10°W to N10°E for (A) the SRFs and (B) the PRFs (using the standard AK135 velocity model, corrected for a 65 km thick crust and with stations elevation taken into account). Outside of the Lhasa terrane, the colour code is artificially faded. Red (resp. blue) colour stands for downwards positive (resp. negative) velocity gradient. The black line segments in (A) beneath the station symbols (open triangles) and the attached numbers (from 1 to 9) give the position of the nine measurements whose results are reported in Table 2 from lines 1–9. The hatched area underlines the extension of the eclogites. The black open dots at horizontal distances between 100 and 150 km and at 60–80 km depths show the earthquake cluster determined by Monsalve *et al.* (2006) and approximately projected on the Hi-CLIMB profile. The seismograms in black heavy lines (subplot A) are the mean bootstrap, moveout-corrected stack of SRFs at 10 consecutive stations. The horizontal heavy black segment attached to the seismograms gives the amplitude scale (whole scale = ±6 per cent of direct *S*-wave amplitude) of the stacked RFs, time is converted to depth using the same velocity model as for the migration.

method is then applied to the Moho using 40 bootstrap samples extracted from the RFs set. For each bootstrap sample of the considered RFs set (PRFs or SRFs), the parameters of the upper layer are chosen following the Gaussian distributions previously found. These parameters are used to compute the contribution of the upper layer to the traveltime of each phase (converted phase and multiples). Figs 8 and 9 illustrate the determination of v_S, κ and h using a set of Hi-CLIMB data (1623 PRFs and 560 SRFs) gained with the 10 stations H1090–H1180. Some differences with the synthetic data example (Figs 2, 4 and 5) exist, not only related to the inescapable seismic noise existing on the real data. First, for the real data, the weights w_{Pi} and w_{Si} ($i = 1, 2, 3$; eqs 7 and 8) are not always equal to 1, the effective used weights depend on the relative strength of the direct conversions and the multiples and on the focusing of the stacks (see Fig. 10 for an example of weight determination with the SRFs). Second, the $h(v_S)$ curves are no longer secant, and a discrepancy of ∼2 km appears in the thickness of the two layers, may be due to a weak dipping of the layers.

RESULTS: ECLOGITES IN THE SOUTHERN LHASA TERRANE LOWER CRUST

The two vertical sections gained with the common conversion point (CCP) migration of the PRFs and the SRFs (for the method, see Wittlinger & Farra (2007)), both along the same profile oriented N10°E and centred at 30.5°N–85.0°E, clearly show the existence, specifically north of the Yarlung Tsangpo Suture (YTS) of a strong converter in the lower crust at about 55–60 km depth (Fig. 7) (the depths are given with the sea level as reference, but the migrated sections are plotted with the ground level as reference, the mean topographic elevation of the Lhasa terrane being ∼5 km). This interface, associated with the Moho at ∼75 to ∼78 km depth, may correspond to the 'lower crustal doublet' already revealed as well at ∼450 km more eastwards (INDEPTH east and west data; Kind *et al.* 2002, Wittlinger *et al.* 2004a) as at ∼200 km more eastwards (HIMNT data; Schulte-Pelkum *et al.* 2005) (Fig. 6). Moreover, at ∼450 km more westwards, beneath the Aksai Chin in most Western Tibet, this doublet also seems to exist (the Sino–French experiment in Western Tibet, Wittlinger *et al.* 2004b). These observations plead for the existence over ∼1000 km of east–west extension of a first-order continuous structure in the lower crust of the Southern Tibet. With the Hi-CLIMB data set, and especially with the SRFs that are not blurred by multiples, the upper converter of the doublet appears first at about 100 km south of the YTS and may be thus interpreted as the top of the Indian lower crust (ILC) underplated beneath the Tibetan crust (Schulte-Pelkum *et al.* 2005; Hetényi *et al.* 2007). On the migrated section gained with the PRFs, which is probably blurred by some upper-crust interface reverberations that may partially 'fade' the direct deeper conversions, the top interface of the ILC is not as clearly imaged. Nevertheless, north of the YTS, the CCP migration of the PRFs simultaneously using the direct conversions and the multiples (Hetényi 2007) evinces that, if on the top interface of the ILC, the direct *P*-to-*S* conversions are weak, in contrary, the multiples are strong, enabling the use of the grid search method.

Deciphering the migrated sections gives thus some clear evidences of the underplating of the ILC beneath the Southern Tibetan crust, but provides no information on the seismic velocities

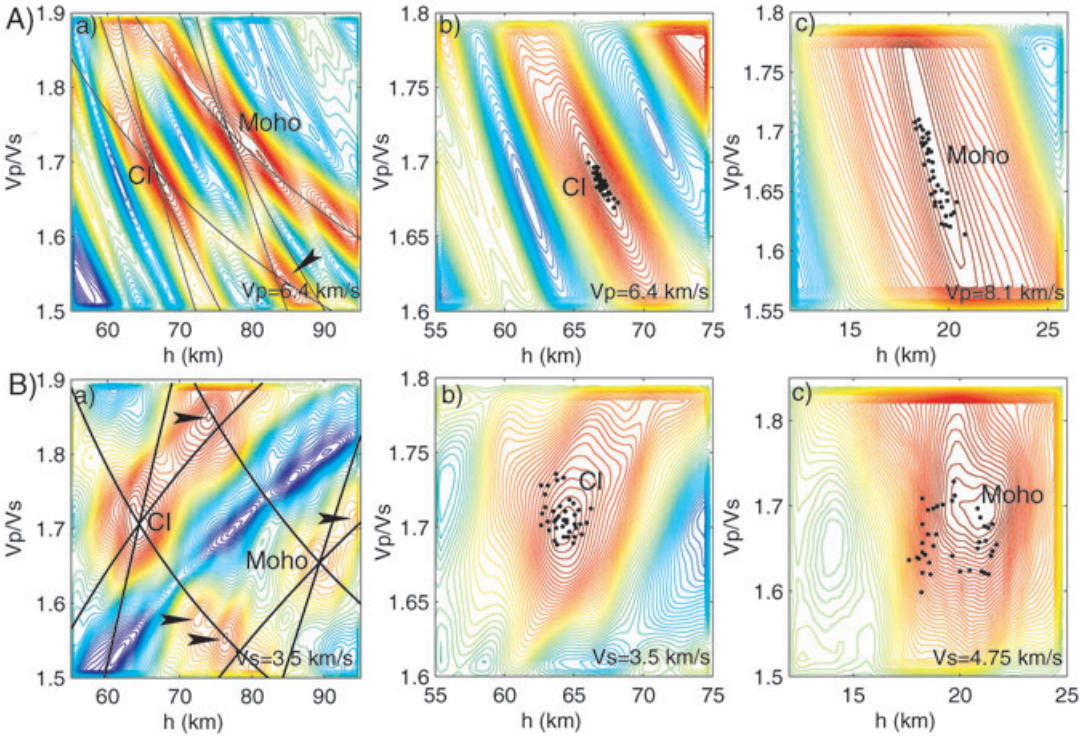

Figure 8. Same as Fig. 2, but for a set of real PRFs (A) and SRFs (B) gained with stations H1090–H1180. Subplots (a) correspond to the whole crust, showing the optimums related to the CI and the Moho as well as (especially for the SRFs) spurious optimums (black pointers). Subplots (b) are the grid search diagrams focused on the upper crust, (c) are the grid search diagrams restricted to the lower crust applying the layer stripping approach. The little black dots in subplots (b) and (c) are the 40 optimums picked on the grid search stacks obtained with the 40 bootstrap RFs samples. While the picking results are very stable for the UCL either with the PRFs or SRFs, significant dispersion appears for the Moho interface due to the parameters errors propagation.

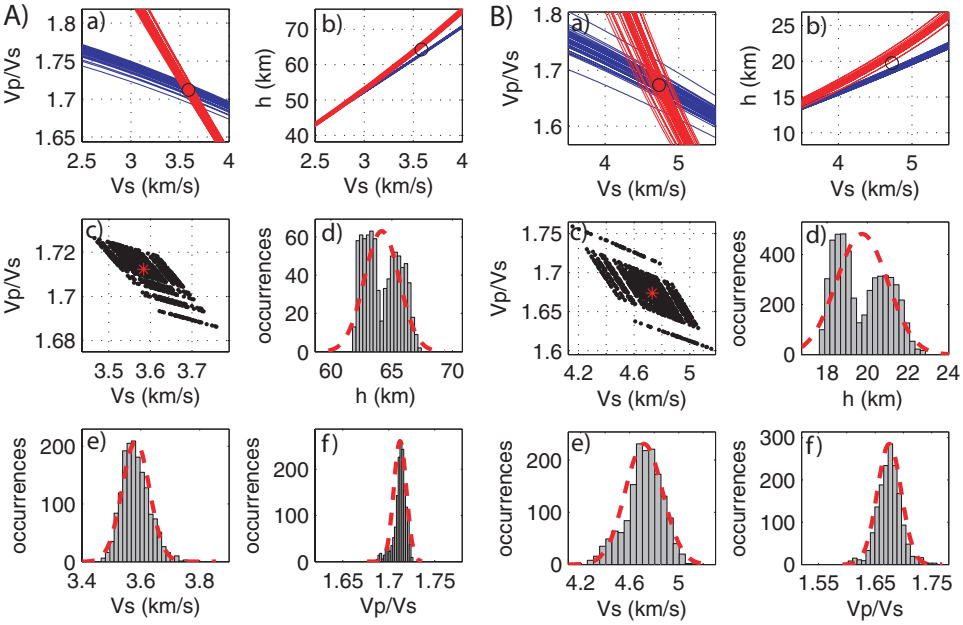

Figure 9. Same as Figs. 4 and 5, but for the Hi-CLIMB data gained with stations H1090–H1180.

variations and hence on the petrological transformations that may occur during the burying of the ILC. Remains now to measure the seismic velocities prevailing in this layer using the grid search method described above. The determination of the parameters v_S, κ and h in the ILC is only possible if the grid search technique can be applied to both, the upper and the lower interface of the ILC. Due to the absence or at least due to the weakness of the conversions at the upper interface of the ILC for one of the two kinds of RFs, generally for the PRFs, the determination of v_S, κ and h could only be achieved accurately for the stations labelled from H1040 to H1230 (the station locations are shown in Figs 6 and 7). At the place where the ILC is buried with a steep angle, somewhere at ∼100 km south

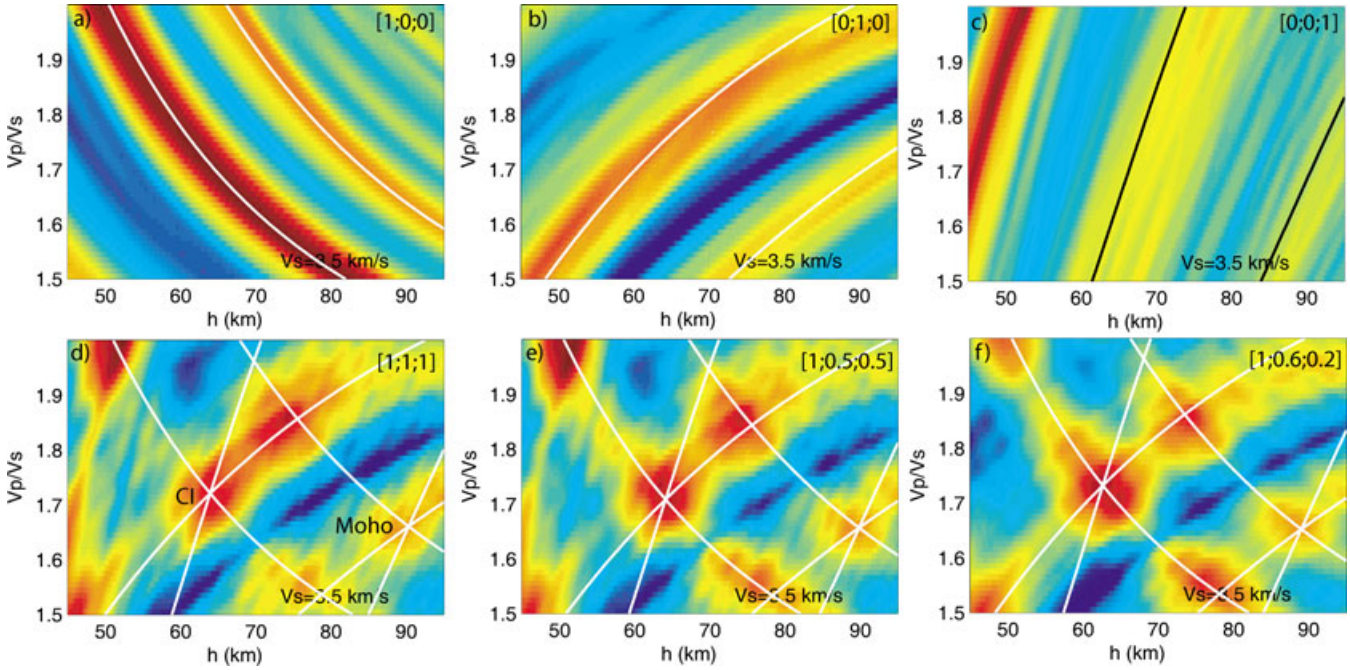

Figure 10. Grid search stacking of the SRFs relative to the stations H1090–H1180 illustrating how the weights w_{Si} in eq. 8 are determined. (a) Only the direct *S*-to-*P* conversions are taken into account (weights are [1, 0, 0]) (b) Only the first multiples *Spsp* + *Sspp* are stacked (weights are [0, 1, 0]).(c) Only the second multiple *Sssp* is stacked (weights are [0, 0, 1]). The colour scale is the same for the three subplots. In this specific example, though the direct *Sp* conversions and the *Spsp* + *Sspp* multiples for both the LCI and the Moho are well focused (subplots a and b), the *Sssp* multiples generated by the LCI and the Moho (subplot c) are poorly focused, especially for the LCI. (d) Final grid search stack using the direct conversion and the two kinds of multiples allocating equal weights [1, 1, 1] to all phases. (e) Same as (d) but using the weights [1, 0.5, 0.5]; (f) same as (d) with weights [1, 0.6, 0.2] giving clear focusing of the stack function. This figure shows that mostly, a large range of weights may be used before severely affecting the results.

of the YTS, the grid search measurements can only be performed for the Moho interface due to the lack in the PRFs of coherent conversions at the top of the ILC, albeit the SRFs CCP migration shows the descending ILC fairly well. The mean value of v_S ($v_S \sim 3.19 \pm 0.10$ km s^{-1}) we determine for the whole crust just around and south of the YTS (stations H0750–H1030) is clearly lower than the mean value ($v_S \sim 3.56 \pm 0.13$ km s^{-1}) we determine north of the YTS (for stations H1040–H1230) for solely the upper ∼60 km of the crust. This observation precludes the existence of a significant shear wave velocity increase in the ILC south of the YTS since the mean value for the whole crust is not raised. North of station H1230, the 'doublet' signature disappears on both migrated sections (Fig. 7), and the determination of the shear wave velocity, κ and thickness can only be performed for the whole crust. Here again, as south of the YTS, the mean shear wave velocity for the whole crust ($v_S \sim 3.65 \pm 0.09$ km s^{-1}) is not significantly raised as compared to the velocity of the upper crust beneath stations H1040–H1230, and hence supports the absence of a high-velocity layer in the lower crust.

We now focus on the crust of the Southern Lhasa terrane where the 'doublet' is observed. For stations H1040 (∼20 km north of the YTS) to station H1230 (∼150 km north of the YTS), the measures can be performed on both the upper and the lower interface of the ILC and enable the determination of the velocities and thickness of the ILC. Six sets of data for stations H1040–H1230, each one ensuing from approximately 10 consecutive stations, with a large overlapping of the data, are used (Figs 6 and 7). Table 2 gives the values (mean and standard deviation) of v_S, κ and layer thickness h obtained with the grid search stacking method combined with the 'layer stripping approach'. We thus first measure v_S, κ and h of the upper/middle crust located above the lower crustal layer. The corresponding RFs are of high quality, which leads to an accurate determination of the three parameters (see Fig. 9a). In addition, the separate processing of the six data sets gives quite similar results. This is an important issue since we use these values in the next step to determine the velocities and thickness of the lower crustal layer. For the lower crustal layer, the six data sets also provide similar results (Table 2). The processing of the whole RFs set obtained at stations H1040–H1230 gives us the following values: for the upper layer, $v_S = 3.56 \pm 0.13$ km s^{-1}, $\kappa = 1.70 \pm 0.02$ and $h = 63.2 \pm 4.1$ km, and for the lower layer, $v_S = 4.73 \pm 0.27$ km s^{-1}, $\kappa = 1.69 \pm 0.06$ and $h = 19.3 \pm 2.4$ km. The values of v_S and κ measured in the upper/middle crust of the Southern Lhasa terrane are quite low as compared to the global average. These results may be summarized (see the sketch in Fig. 11) with two main statements: (1) the ILC undergoes a huge increase of its shear wave velocity v_S and (2) this increase is restrained to an area extending northwards from about 20 km north of the YTS to ∼150 km north of the YTS corresponding to the hatched surface area in Fig. 6. Such a high shear wave velocity is typical for eclogites (Bascou *et al.* 2001; Gao *et al.* 2001; Kopylova *et al.* 2004) and more marginally for granulites.

Remains the question of distinguishing eclogites from mafic granulites or other ultra mafic rocks. This may be achieved in part by considering the κ parameter, sensitive to hydration of the rocks and also to the presence of some specific minerals having a very low Poisson's ratio, for example quartz. If during exhumation and exposure hydration can take place thus raising the κ-value of exposed eclogites, then at greater depth the hydration of eclogites seems to be weak (H_2O < 1wt. per cent) (Gao *et al.* 2001). Measurements on

Table 2. Results of grid search stacking of PRFs and SRFs combined with the 'layer stripping approach' for the Lhasa terrane along the Hi-CLIMB profile.

Stations	Upper and middle crust	Lower crust
(1) H0750–H1030	$v_S = 3.19 \pm 0.1$ km s^{-1} $\kappa = 1.70 \pm 0.01$ $h = 68.8 \pm 2.5$ km	No measure
(2) H1040–H1130 v_S (rms whole crust) = 3.74 km s^{-1}	$v_S = 3.48 \pm 0.08$ km s^{-1} $\kappa = 1.72 \pm 0.01$ $h = 56.3 \pm 5.7$ km	$v_S = 4.63 \pm 0.25$ km s^{-1} $\kappa = 1.73 \pm 0.03$ $h = 19.2 \pm 3.7$ km
(3) H1070–H1150 v_S (rms whole crust) = 3.76 km s^{-1}	$v_S = 3.46 \pm 0.09$ km s^{-1} $\kappa = 1.72 \pm 0.01$ $h = 61.5 \pm 1.4$ km	$v_S = 4.85 \pm 0.10$ km s^{-1} $\kappa = 1.71 \pm 0.02$ $h = 19.9 \pm 0.8$ km
(4) H1090–H1180 v_S (rms whole crust) = 3.83 km s^{-1}	$v_S = 3.58 \pm 0.05$ km s^{-1} $\kappa = 1.71 \pm 0.01$ $h = 64.2 \pm 1.4$ km	$v_S = 4.72 \pm 0.15$ km s^{-1} $\kappa = 1.68 \pm 0.02$ $h = 20.5 \pm 1.7$ km
(5) H1110–H1200 v_S (rms whole crust) = 3.88 km s^{-1}	$v_S = 3.67 \pm 0.13$ km s^{-1} $\kappa = 1.69 \pm 0.01$ $h = 66.3 \pm 2.4$ km	$v_S = 4.72 \pm 0.10$ km s^{-1} $\kappa = 1.68 \pm 0.02$ $h = 18.9 \pm 1.8$ km
(6) H1140–H1230 v_S (rms whole crust) = 3.85 km s^{-1}	$v_S = 3.66 \pm 0.06$ km s^{-1} $\kappa = 1.68 \pm 0.01$ $h = 67.0 \pm 2.4$ km	$v_S = 4.63 \pm 0.12$ km s^{-1} $\kappa = 1.76 \pm 0.03$ $h = 18.3 \pm 1.3$ km
(7) H1160–H1230 v_S (rms whole crust) = 3.77 km s^{-1}	$v_S = 3.52 \pm 0.09$ km s^{-1} $\kappa = 1.71 \pm 0.01$ $h = 64.4 \pm 1.6$ km	$v_S = 4.73 \pm 0.13$ km s^{-1} $\kappa = 1.66 \pm 0.03$ $h = 19.2 \pm 2.9$ km
(8) H1240–H1340	$v_S = 3.65 \pm 0.09$ km s^{-1} $\kappa = 1.71 \pm 0.01$ $h = 70.3 \pm 1.6$ km	No measure
(9) H1350–H1420	$v_S = 3.64 \pm 0.08$ km s^{-1} $\kappa = 1.80 \pm 0.01$ $h = 70.3 \pm 1.5$ km	No measure

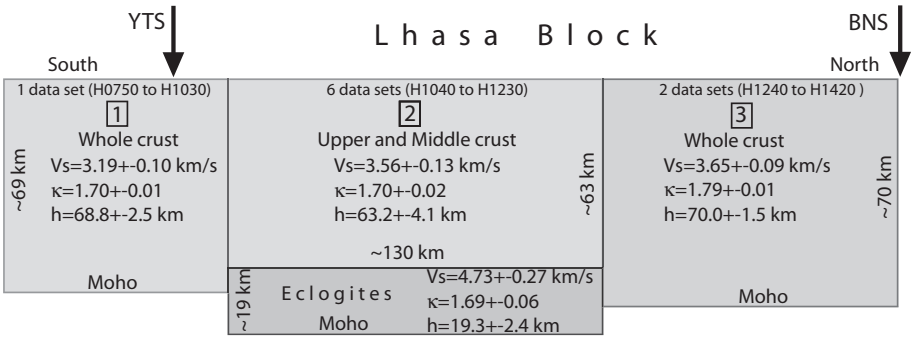

Figure 11. Summary sketch of the results (v_P, κ and h) obtained using (1) one data set for stations H0750–H1030, (2) six data sets for stations H1040–H1230 and (3) two data sets for stations H1240–H1420.

samples (Gao *et al.* 2001; Kern *et al.* 1999) show that eclogites have a rather low κ-value (<1.71) simultaneously due to the presence of quartz and due to the weak hydration, while for mafic granulites κ is significantly higher (>1.78) and only marginally higher for other ultra mafic rocks. Our results for the high-velocity layer ($v_S \sim 4.73$ km s^{-1}; $\kappa \sim 1.69$) are very close for v_S and κ to the results obtained for some samples from the Dabie Shan sites, China (Gao *et al.* 2001) ($v_S \sim 4.74$ km s^{-1}; $\kappa \sim 1.70$) corresponding to weak hydration ($\sim$0.68wt. per cent of H_2O). The modal composition shows that the quartz mineral seems not to be abundant in these samples albeit the measured low κ-value. Probably a low κ-value can also result from a weak hydration alone. The highest value of the κ parameter we may expect in the lower crust layer, with only a low probability of occurrence, is $\sim$1.75. This value remains still at the lower limit of the mafic granulites κ-values ($\sim$1.78). On the other hand, the lower bound of v_S ($\sim$4.46 km s^{-1}) expected in the lower crust layer is still higher than the upper bound of the shear velocity ($\sim$4.20 km s^{-1}) in mafic granulites (Rudnick & Fountain 1995).

From Bouguer anomaly inversion and petrological modelling, Hetényi *et al.* (2007) conclude that the hydration (∼1wt. per cent H_2O) is weak in the lower crust layer in agreement with the low κ-value (∼1.69) we obtain here. In addition, Hetényi *et al.* (2007) find a very high density (3300 kg m^{-3}) for the rocks of this lower crust layer; this value is in agreement with the density value (3370 kg m^{-3}) deduced from our velocity determinations using Birch's law approximation.

The eclogitization process initiates if high pressures, rather high temperatures and first of all hydrous fluids are present (John & Schenk 2003). If the required temperatures (∼600° to ∼700°) and pressures (∼15 to ∼20 kbars) are plausible in the lower crust at ∼60 km depth beneath southern Tibet (Mechie *et al.* 2004), the origin of the hydrous fluids remains debatable. Water released by mineral dehydration may be in some cases sufficient to trigger eclogitization (Rubie 1998), but Jackson *et al.* (2004) propose another mechanism in which the hydrous fluids may infiltrate through the fractures induced by local earthquakes. In the meantime, combined gravity, thermo-kinematic and petrological modelling shows that the eclogitization process in Southern Tibet is delayed until dehydration reaction occurs, and the freed fluids may cause local earthquakes (Hetényi *et al.* 2007). This latter mechanism seems to be plausible beneath Southern Tibet plateau. In fact, some 200 km east of the Hi-CLIMB profile (between ∼86° and ∼88°E) deep earthquakes are localized near the Moho in the lowermost crust or uppermost mantle approximately beneath the YTS (Monsalve *et al.* 2006; reported in Fig. 7 as well), coinciding with the modelled location of delayed eclogitization. Until now no information on the existence of similar deep earthquakes beneath the Hi-CLIMB profile (∼85°E) is available, but considering provisional regional earthquake catalogues (Laugin *et al.* 2003) we may reasonably expect that a similar cluster of deep earthquakes also exists beneath the YTS at about 85°E at the place where the southern edge of the eclogite pillow is detected.

CONCLUSION

The grid search stacking method applied on many bootstrap-selected sets of both PRFs and SRFs allowed us to determine the effective shear wave velocity, v_P/v_S ratio and thickness of piled-up layers in the Tibetan crust. We conclude, owing to the high shear wave velocity, the high density and the rather low v_P/v_S ratio that the lower crust, between ∼63 and ∼82.5 km depth, extending northwards from ∼20 to ∼150 km north of the YTS (in Fig. 6 the crisscrossed hatched area) is composed of eclogites. Above and beside this eclogitic layer we do not detect any evidence of high shear wave velocity and high v_P/v_S ratio that would reveal the existence of widespread mafic rocks. This leaves little room for a transformation process from eclogite to granulite that would have taken place in the middle crust of the Southern Lhasa terrane (Schulte-Pelkum *et al.* 2005).

What is then the fate of this deep, about 19 km thick, almost horizontal eclogitic layer? Due to their high density a slow foundering of the eclogites into the mantle cannot be ruled out (Johnson 2002). The only evidence indicating that such a scenario may be presently in progress is the ∼13-km deeper Moho beneath the eclogites than further north. However, this would imply an en bloc sinking of the eclogitic layer in the mantle since the Moho beneath is quasi horizontal. A foundering with a parrot beak shape at the northern edge of the eclogitic layer would rather be expected, but no evidence of such a process is seen on the migrated sections. The amount of lower (former Indian) crust that has been eclogitized and may potentially disappear into the mantle plays a fundamental role in partitioning between lateral extrusion and vertical rock-mass transfer to explain the deficit in thickening of the Tibetan crust.

ACKNOWLEDGMENTS

We are grateful for the constructive and helpful remarks of an anonymous referee. All the people involved in the servicing of the Hi-CLIMB network and those who prepared the data set should find here our furthest acknowledgment.

REFERENCES

Bascou, J., Barruol, G., Vauchez, A., Mainprice, D. & Egydio-Silva, M., 2001. EBSD-measured lattice-preferred orientations and seismic properties of eclogites, *Tectonophysics,* **342,** 61–80.

Dix, C.H., 1955. Seismic velocities from surface measurements, *Geophysics,* **20,** 68–86.

England, P. & Houseman, G., 1989. Finite strain calculation of continental deformation, 2. Comparison with India-Asia collision zone, *J. geophys. Res.,* **91**(B3), 3664–3676.

Gao, S., Kern, H., Jin, Z.M., Popp, T., Jin, S.Y., Zhang, H.F. & Zhang, B.R., 2001. Poisson's ratio of eclogite: the role of retrogression, *Earth planet. Sci. Lett,* **192,** 523–531.

Haines, S.S. *et al.*, 2003. INDEPTH III seismic data: from surface observations to deep crustal processes in Tibet, *Tectonics* **22**(1), doi:10.1029/2001TC001305.

Henry, P., Le Pichon, X. & Goffé, B., 1997. Kinematic, thermal and petrological model of the Himalayas: constraints related to metamorphism within the underthrust Indian crust and topographic elevation, *Tectonophysics,* **273**(1-2), 31–56.

Hetényi, G., 2007. Evolution of deformation of the Himalayan prism: from imaging to modelling, *Ph.D thesis*. Université Paris XI, Ecole Normale Supérieure, Paris, pp. 400.

Hetényi, G., Cattin, R., Brunet, F., Bollinger, L., Vergne, J., Nábělek, J.L. & Diament, M., 2007. Density distribution of the India plate beneath the Tibetan plateau: geophysical and petrological constraints on the kinetics of lower-crustal eclogitization, *Earth planet. Sci. Lett.,* **264,** 226–244, doi:10.1016/j.epsl.2007.09.036.

Jackson, J.A., Austrheim, H., McKenzie, D. & Priestley, K., 2004. Metastability, mechanical strength and the support of mountain belts, *Geology*, **32**(7), 625–628.

John, T. & Schenk, V., 2003. Partial eclogitisation of gabbroic rocks in a late Precambrian subduction zone (Zambia): prograde metamorphism triggered by fluid infiltration. *Contrib. Meneral. Petrol.,* **146**(2), 174–191.

Johnson, M.R.W., 2002. Shortening budgets and the role of continental subduction during the India-Asia collision, *Earth Sci. Rev.,* **59,** 101–123.

Kern, H., Gao, S., Jin, Z., Popp, T. & Jin, S., 1999. Petrophysical studies on rocks from the Dabie ultrahigh-pressure (UHP) metamorphic belt, Central China: implications for the composition and delamination of the lower crust, *Tectonophysics,* **301,** 191–215.

Kind, R. *et al*., 2002. Seismic images of the crust and upper mantle beneath Tibet: evidence for Eurasian plate subduction. *Science,* **298**(5596), 1219–1221.

Kopylova, M.G., Lo, J. & Christensen, N.I., 2004. Petrological constraints on seismic properties of the Slave upper-mantle (Northern Canada), *Lithos,* **77,** 493–510, doi:10.1016/j.lithos.2004.03012.

Laugin, W.R., Brown, L.D. & Sandvol, E.A., 2003. Seismicity of Central Tibet from Project INDEPTH III seismic recordings, *Bull. seism. Soc. Am.,* **93–5,** 2146–2159, doi:10.1785/0120030004.

Le Pichon, X., Fournier, M. & Jolivet, L., 1992. Kinematics, topography, shortening and extrusion in the India-Eurasia collision, *Tectonics,* **11,** 1085–1098.

Le Pichon, X., Henry, P. & Goffé, B., 1997. Uplift of Tibet: from eclogites to granulites; implications for the Andean Plateau and the Variscan belt, *Tectonophisics,* **273**(1–2), 57–76.

Lombardi, D., Braunmiller, J., Kissling, E. & Giardini, D., 2008. Moho depth and Poisson's ratio in the Western-Central Alps from receiver functions, *Geophys. J. Int.,* doi:10.1111/j.1365-146X.2007.03706.x.

Mechie, J. *et al.,* 2004. Precise temperature estimation in the Tibetan crust from seismic detection of the a-b quartz transition, *Geology,* **32–7,** 601–604, doi:10.1130/G20367.1.

Monsalve, G., Sheehan, A., Schulte-Pelkum, V., Rajaure, S., Pandey, M.R. & Wu, F., 2006. Seismicity and one-dimensional velocity structure of the Himalayan collision zone: earthquakes in the crust and upper mantle. *J. geophys. Res.,* **111**(B10), B110301.

Monsalve, G., Sheehan, A., Rowe, C. & Rajaure, S., 2008. Seismic structure of the crust and the upper mantle beneath the Himalayas: evidence for eclogitization of lower crustal rocks in the Indian Plate. *J. geophys. Res.,* **113,** B08315, doi:10.1029/2007JB005424, 2008.

Nábělek, J., Vergne, J., Hetényi, G. & Hi-CLIMB team, 2005. Project Hi-CLIMB: a synoptic view of the Himalayan Collision Zone and Southern Tibet, *Eos, Trans. AGU,* **86**(52), Fall Meet. Suppl. Abstract T52A-02.

Owen, T. & Zandt, G., 1997. Implications of crustal property variations for models of Tibetan plateau evolution, *Nature,* **387,** 37–43.

Peltzer, G. & Tapponnier, P., 1988. Formation and evolution of strike-slip faults, rifts and basins during the India–Asia collision: an experimental approach, *J. geophys. Res.,* **93,** 15085–15117.

Rubie, D., 1998. Disequilibrium during metamorphism: the role of nucleation kinetics, in *What Drives Metamorphism and Metamorphic Reactions?,* Vol.138, 199–214, eds P. Treloar & P. O'Brien, *Geol. Soc. London, Spec. Publ*.

Rudnick, R.L. & Fountain, D.M., 1995. Nature and composition of the continental crust: a lower crustal perspective, *Rev. Geophys.,* **33**(**3**), 267–309.

Sapin, M. & Hirn, A., 1996. Seismic structure and evidence for eclogitization during the Himalayan convergence, *Tectonophysics,* **273**(1-2), 1–16.

Schulte-Pelkum, V., Monsalve, G., Sheehan, A., Pandey, M.R., Sapkota, S., Bilham, R. & Wu, F., 2005. Imaging the Indian subcontinent beneath the Himalaya, *Nature,* **345**(30), 1222–1225, doi:10.1038/nature03678.

Tapponnier, P. & Molnar, P., 1977. Active Faulting and tectonics in China, *J. geophys. Res.,* **82,** 2905–2930.

Wittlinger, G. & Farra, V., 2007. Converted waves reveal a thick and layered tectosphere beneath the Kalahari super-craton, *Earth planet. Sci. Lett.,* **254,** 404–415, doi:10.1016/j.epsl.2006.11.048.

Wittlinger, G., Farra, V. & Vergne, J., 2004a. Lithospheric and upper mantle stratifications beneath Tibet: new insights from Sp conversions, *Geophys. Res. Lett.,* **31**(19), L19615.

Wittlinger, G. *et al*., 2004b. Teleseismic imaging of subducting lithosphere and Moho offsets beneath western Tibet, *Earth planet. Sci. Lett.,* **221**(1-4), 117–130.

Zhu, L.P. & Kanamori, H., 2000. Moho depth variation in southern California from teleseismic receiver functions, *J. geophys. Res.,* **105,** 2969–2980.